Available online at www.sciencedirect.com

jmr&t Journal of Materials Research and Technology

journal homepage: www.elsevier.com/locate/jmrt

In situ fabrication of spherical oxide dispersion strengthened Ti powder through gas atomization

Hyeon-Tae Im [a,b], Woo Jin Kim [c], Nam-Seok Kim [d], Dae Ha Kim [e], Chang-Soo Park [a], Kwangsuk Park [a], Young Do Kim [b,*,1], Hyung-Ki Park [a,**,1]

[a] Functional Materials and Components R&D Group, Korea Institute of Industrial Technology, Gangneung 25440, Republic of Korea

[b] Division of Materials Science and Engineering, Hanyang University, Seoul 04763, Republic of Korea

[c] Department of Materials Science and Engineering, Hongik University, Seoul 121-791, Republic of Korea

[d] Industrial Materials Processing R&D Department, Korea Institute of Industrial Technology, Incheon 21999, Republic of Korea

[e] KONASOL R&D Center, KONASOL, Dangjin 31806, Republic of Korea

ARTICLE INFO

Article history:
Received 2 March 2023
Accepted 9 May 2023
Available online 13 May 2023

Keywords:
Titanium
Oxide dispersion strengthened alloy
Powder
In situ fabrication
Oxidation driving force

ABSTRACT

Oxide dispersion strengthened (ODS) alloys exhibit excellent mechanical properties due to fine oxide dispersion, but they have great limitations due to utilizing powder fabrication via mechanical alloying. Therefore, this study examined the alloy composition and process that can fabricate ODS titanium (Ti) powder in situ through a gas atomization method. The composition and content of the oxide, which can dissolve in molten Ti during melting and precipitate inside powders during cooling in the gas atomization, were derived through thermodynamic calculations. The ODS Ti alloy composition of Ti + 1 wt% yttria (Y_2O_3) was derived, and the alloy was prepared as a powder through an electrode induction melting gas atomization (EIGA) method. First, rod-shaped ingots were prepared through vacuum arc remelting (VAR), and Y_2O_3 was coarsely precipitated along the grain boundaries due to the slow cooling rate. Then, the ODS Ti powder was fabricated by EIGA using the rod ingot and spherical powders could be continuously fabricated. The cross-section microstructure of the powder was observed, and the Y_2O_3 particles with several tens of nm were uniformly distributed inside the powder. These thermodynamic calculations and experiments confirmed that ODS Ti powder could be fabricated in situ using the gas atomization method.

* Corresponding author.
** Corresponding author.
E-mail addresses: ydkim1@hanyang.ac.kr (Y.D. Kim), mse03@kitech.re.kr (H.-K. Park).
[1] Hyung-Ki Park and Young Do Kim equally contributed to this work.

https://doi.org/10.1016/j.jmrt.2023.05.097

1. Introduction

Titanium (Ti) and its alloy have excellent specific strength and corrosion resistance, making it widely used in the aerospace and chemical plant industries [1–3]. In addition, because they exhibit outstanding biocompatibility in an *in vivo* environment, they are applied as materials for medical implant parts [4–6]. However, in contrast to the advantages, Ti alloys have problems, such as low wear resistance and fatigue properties, compared to other metallic alloys [7,8]. Moreover, using Ti alloys for high-temperature parts is limited because their mechanical properties rapidly deteriorate with increasing temperatures [9].

An oxide dispersion strengthened (ODS) alloy is an alloy in which fine oxide particles with sub-micron size are dispersed in a metal matrix [10–12]. The ODS alloys exhibit high strength and hardness because the movements of dislocations and grain boundaries are suppressed by oxide particles [13,14]. In addition, wear resistance can be increased by dispersing oxide particles with high hardness and low friction coefficients [15,16]. Besides, there is an advantage in maintaining high mechanical properties even at high-temperature due to the high thermal stability of the oxide [17,18]. Therefore, numerous studies have been conducted on the oxide dispersion strengthening effect in various metallic alloy systems, and some research on ODS Ti alloys have been reported [19,20].

Li et al. [19] reported a study on an ODS Ti alloy in which yttria (Y_2O_3) was dispersed in a Ti–6Al–4V alloy. In the room temperature (RT) compression test, the yield and compressive strength of the conventional Ti–6Al–4V alloy were 880 and 1227 MPa, respectively. When 1 wt% Y_2O_3 was added to the Ti–6Al–4V alloy, the yield and compressive strength significantly increased to about 1100 and 1400 MPa while maintaining the plastic strain. In the high-temperature compression test at 450 °C, the yield and compressive strength of the Ti–6Al–4V + 2 wt% Y_2O_3 alloy were 832 and 1088 MPa, respectively, showing much higher strength than the Ti–6Al–4V alloy. Li et al. [20] reported changes in the mechanical properties and biocompatibility of commercially pure Ti by adding oxides. When zirconia (ZrO_2) and silica (SiO_2) were added to the pure Ti, the RT compressive strength increased significantly. In addition, in cell growth experiments, it was reported that cell adhesion and growth characteristics were superior to the ODS Ti alloys compared to the pure Ti. In previous studies, ODS Ti alloy powders were prepared by high-energy milling of Ti and oxide powders, and bulk samples were fabricated through a spark plasma sintering method [19,20]. However, there is a great limitation in the fabrication of ODS alloys by this sample preparation method.

Since the density difference between oxides and metals is large, when ODS alloys are fabricated through a conventional casting method, the oxide floats in the molten metal, causing non-uniform distributions. Accordingly, the ODS alloys are normally fabricated by powder metallurgy, and ODS alloy powders are prepared by mechanical alloying (MA) methods, such as high-energy milling, to disperse oxides uniformly [21,22]. However, the MA method suffers from not only extremely low productivity but also the contamination of oxygen (O) and iron (Fe) from the milling container [23]. Furthermore, the ODS powder prepared by the MA method cannot apply to an additive manufacturing (AM) process due to its highly irregular morphology [24,25]. Despite the ODS alloy's excellent mechanical properties, it is difficult to commercialize because of major drawback in the fabrication method.

If high-quality spherical ODS powders can be easily manufactured in large quantities, the above mentioned limitations of the ODS alloys can be overcome. Therefore, this study examined the alloy composition and process technology for the in situ fabrication of spherical ODS Ti powder. Through thermodynamic calculations, the oxide composition and content that can form oxides inside the Ti powder during gas atomization were derived. The designed alloy was prepared as powders through an electrode induction melting gas atomization (EIGA) method, and the powder morphology and oxide distribution inside the powders were examined.

2. Materials and methods

Initial Ti + 1 wt% Y_2O_3 alloy ingots were prepared by vacuum arc re-melting (VAR) using Ti lump (99.99% purity, RND KOREA) with the size less than 10 mm and Y_2O_3 powders (99.99% purity, RND KOREA) with an average size of 4.5 μm. The O concentration of the Ti lump was 0.1 wt%, and the purity of the Y_2O_3 powder was 99.99 wt%. Afterward, the Ti + 1 wt% Y_2O_3 alloy will be designated as Ti(0.1O)–1Y_2O_3. The ingots were re-melted five times while turning the ingot upside down to prepare ingots with uniform compositions. Firstly, the Ti(0.1O)–1Y_2O_3 alloy ingots were fabricated as 70 × 20 mm (diameter × height) disc samples using the water-cooled copper crucible.

To fabricate Ti(0.1O)–1Y_2O_3 alloy powders by the EIGA method, a rod-shaped ingot was cast in a water-cooled copper crucible with the size of 30 × 200 mm (diameter × height) using the disc-shaped ingot samples. The powder was fabricated using the Ti(0.1O)–1Y_2O_3 rod ingot sample by the EIGA (Force Metal, NEV-FFGA2T). The EIGA chamber was purged with high-purity argon gas and evacuated to remove residual O. Then, 70 kW power was applied to the induction coil to melt the rod ingot, and argon gas was sprayed at 50 bar to molten metal droplets for the powder fabrication. The atomized powder was sieved with meshes ranging from 46 to 150 μm.

The oxidation driving forces of the Ti oxide and the Ti–O solid solution systems below the melting temperature were calculated through the Thermo-Calc software using the SSUB5 and TCTI5 databases. The oxidation driving forces above the melting temperature were used the data from the previous study [24], which represents the oxidation driving forces of Ti above the melting temperature considering the enthalpy change of the solid and liquid phases. In addition, the phase formation behavior and equilibrium phase fraction of the Ti(0.1O)–1Y_2O_3 alloy with respect to the temperature were also calculated.

The yttrium (Y) and O concentration in the rod ingot and powder were analyzed using a wavelength-dispersive X-ray fluorescence (XRF) spectrometer (S8 TIGER, BRUKER) and O/N analyzer (Leco, 736 series), respectively, and the results are

Table 1 – Chemical composition of the Ti(0.1O)–1Y_2O_3 alloy rod ingot and powder (wt%).

	Y	O
Rod ingot	0.787	0.322
Powder	0.786	0.331

presented in Table 1. Meanwhile, the microstructures of the rod ingot and powder were analyzed using a field emission-scanning electron microscope (FE-SEM) (FEI, QUANTA FEG 250) equipped with an energy-dispersive spectrometer (EDS) (EDAX, Octane Elite EDS). For the observation of oxide particles in the powder, the powder was examined via a field emission-transmission electron microscope (FE-TEM) (Titan G2 ChemiSTEM Cs Probe, FEI). A sample for the TEM analysis was prepared by a focused ion beam instrument (Versa 3D DualBeam, FEI).

The hardness of the powder was carried out through a Vickers hardness test (HM-200, Mitutoyo). The hardness was measured in the cross section of the powder by applying a load of 0.01 kg/f and holding for 10 s. To evaluate the degree of hardness increase of the Ti(0.1O)–1Y_2O_3 alloy powder, the hardness of the pure Ti powder with an oxygen concentration of 0.1 wt% was also analyzed. The hardness values were derived as an average value by measuring 10 powders each.

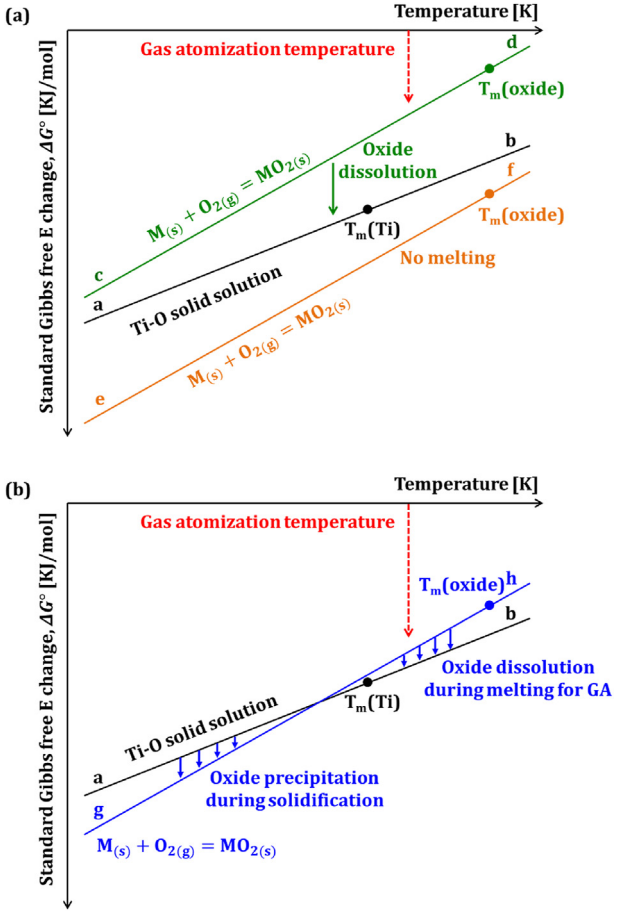

Fig. 1 – Schematic showing an idea for the in situ fabrication of the ODS Ti powder by the gas atomization method.

3. Results and discussion

Fig. 1 is a schematic showing ideas for designing a combination of Ti and oxide that can form oxides inside the Ti powder in situ during the gas atomization process. The schematic represents the standard Gibbs free energy change (ΔG^0) for oxidation reactions with respect to the temperature. In Fig. 1(a), line a-b shows the reaction where O is dissolved in the Ti matrix (Ti–O solid solution) during the oxidation of Ti, while lines c-d and e-f show the reactions where metal was oxidized to form an oxide. Looking at the slope of each line in the figure, the slope of the Ti–O solid solution reaction (line a-b) represents smaller than that of the oxide formation reactions (lines c-d and e-f). The equation of the ΔG^0 for the metal oxidation reaction is as follows

$$\Delta G^0 = \Delta H^0 - T\Delta S^0 \quad (1)$$

where ΔH^0 is the standard enthalpy change and ΔS^0 is the standard entropy change for the oxidation reaction. That is, the slope of the graph is $-\Delta S^0$, and the larger the value of $|\Delta S^0|$, the greater the slope. In the oxidation reaction of metals, $|\Delta S^0|$ tends to increase with increasing the absolute value of volume change ($|\Delta V|$) in the reaction [26,27]. In general, when O is dissolved in the metal matrix while metal is oxidized, O is located at the interstitial site. In this case, volume expansion after oxidation is smaller than when the oxide is formed. Therefore, it is expected that the $|\Delta S^0|$ value of the reaction where O is dissolved in the metal matrix is smaller than that of the reaction where metal is oxidized to form oxides, and for this reason, the slope of line a-b is shown as small.

In Fig. 1(a), point T_m(Ti) represents the melting temperature of Ti. In the gas atomization process, since the powder is fabricated after melting the alloy, the gas atomization temperature indicated in red is shown at a temperature higher than T_m(Ti). If an oxide of an element having a lower oxidation driving force (line c-d) than the Ti–O solid solution is added to Ti, the oxide is decomposed and dissolved in the Ti matrix. On the other hand, if an oxide of an element with a higher oxidation driving force (line e-f) than the Ti–O solid solution is added to Ti, it exists as an oxide even above the T_m(Ti), resulting in the slag formation during melting.

Therefore, the idea shown in Fig. 1(b) was derived to form oxide particles in situ inside the Ti powder in the gas atomization process. When an oxide of an element that has a relationship shown by line g-h with the Ti–O solid solution system is added, the oxidation driving force of the Ti–O system is higher above the T_m(Ti), decomposing the oxide and dissolving in the molten Ti. While cooling in the gas atomization process, the oxidation driving force for the oxide formation reaction (line g-h) is higher than that of the Ti–O solid solution (line a-b), resulting in the re-precipitation of oxides. Thus, if we find a Ti and oxide combination that has the thermodynamic relationship in which the oxide is completely dissolved into molten Ti above the T_m(Ti) and re-precipitated

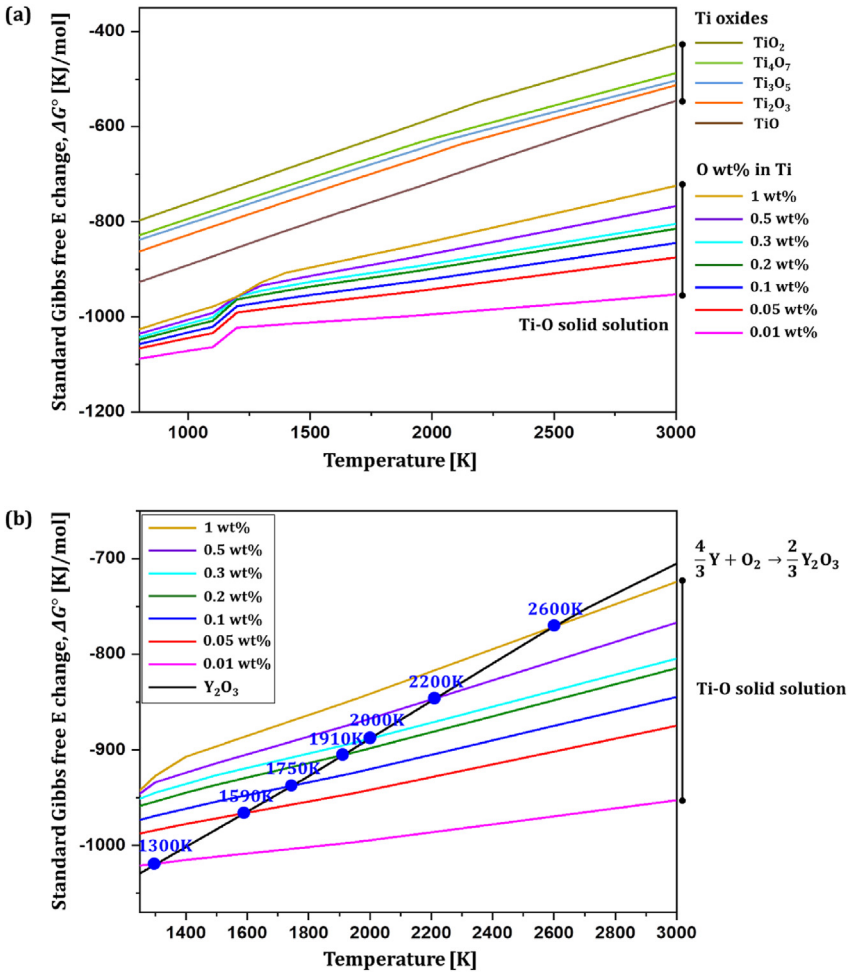

Fig. 2 – (a) Oxidation driving force for reactions of Ti oxide formation and Ti–O solid solution systems and (b) the enlarged view of the oxidation driving force of the Ti–O solid solution system in a high-temperature region. In Fig. 2(b), black line represents the oxidation driving force of Y ($^4/_3\,Y + O_2 \rightarrow {}^2/_3 Y_2O_3$).

during cooling, it will be possible to fabricate the ODS Ti powder in situ during the gas atomization process.

Following the above, the driving forces for the Ti oxidation reactions were calculated first. Fig. 2(a) shows the oxidation driving forces when Ti is oxidized to form oxides and when O is dissolved in the Ti matrix without forming oxides. The grape represents the ΔG^0 with respect to the temperature range from 800 to 3000 K in the oxidation reaction. In the oxidation reaction where Ti forms oxides, the oxidation driving force increases as the fraction of O in the Ti oxide decreases. Comparing the oxidation reactions for the Ti oxides and the Ti–O solid solution systems, the latter has a higher oxidation driving force. Examining the slope meaning – ΔS^0, the Ti–O solid solution systems had a smaller value than the reaction for the oxide formation, as shown in Fig. 1. In the Ti–O solid solution systems, the oxidation driving force varies depending on the O concentration of the Ti matrix, and the lower the O concentration, the higher the oxidation driving force. The slopes in the Ti–O solid solution systems change rapidly around 1200 K, caused by the alpha(α)-beta(β) phase transformation of Ti [28].

As previously mentioned in Fig. 1, if the oxide decomposes into molten Ti during the melting and re-precipitates in the Ti powder matrix during cooling in the EIGA process, the ODS Ti powder can be fabricated in situ. In this case, the oxidation driving force when O is dissolved is important, not when Ti forms oxides. Therefore, the oxidation driving force of the Ti–O solid solution systems at high temperatures is enlarged and shown in Fig. 2(b). To find an oxide with the relationship shown in Fig. 1(b), the optimal oxide was derived by calculating the oxidation driving force for various elements. The colored lines represent the oxidation driving force of the Ti–O solid solution according to the O concentration in Ti matrix, and the black line represents the driving force for the oxidation reaction of Y.

$$^4/_3\,Y + O_2 \rightarrow {}^2/_3 Y_2O_3 \quad (2)$$

The oxidation driving forces of Y and Ti–O solid solution have a relationship as mentioned in Fig. 1(b).

The O concentration of the initial Ti material used in this study was 0.1 wt%. Thus, comparing the oxidation driving forces of Y and Ti–O solid solution system with the O

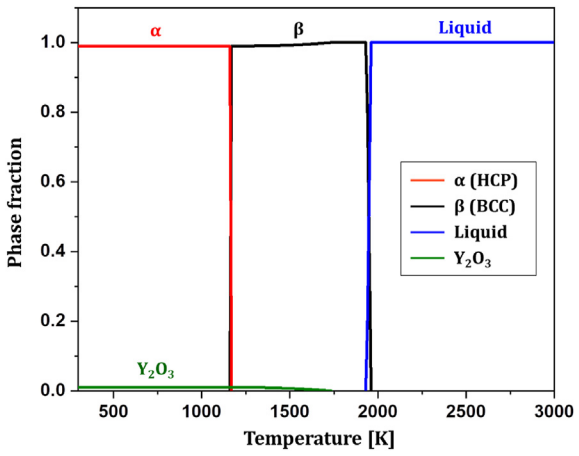

Fig. 3 – Equilibrium phase formation behavior of Ti(0.1O)–1Y_2O_3 (Ti-0.79Y-0.31O, wt%) with respect to temperature. The green and blue lines represent the phase fractions of the Y_2O_3 and liquid phase, respectively.

concentration of 0.1 wt%, the oxidation driving force of the Ti–O solid solution is higher above 1750 K, which temperature is lower than the melting temperature of Ti (1941 K). Therefore, at temperatures above 1750 K, the Y_2O_3 would be reduced and dissolved into the Ti matrix.

$$Ti + Y_2O_3 \rightarrow Ti(O) + Y \quad (3)$$

While, at temperatures below 1750 K, the oxidation driving force of Y is higher, and the O in the Ti matrix would react with Y to form Y_2O_3.

$$Ti(O) + Y \rightarrow Ti + Y_2O_3 \quad (4)$$

Therefore, in the Ti–Y_2O_3 alloy, the Y_2O_3 is decomposed into Ti during melting, and re-precipitated into the Ti matrix during cooling while being atomized, so that the ODS Ti powder can be fabricated in situ by the gas atomization method.

Then, the phase formation behavior according to the temperature was analyzed in the composition of the alloy used in this study. In this study, commercially pure Ti with an O concentration of 0.1 wt% was used and 1 wt% of Y_2O_3 was added to Ti, so the Y and O concentrations in the Ti(0.1O)–

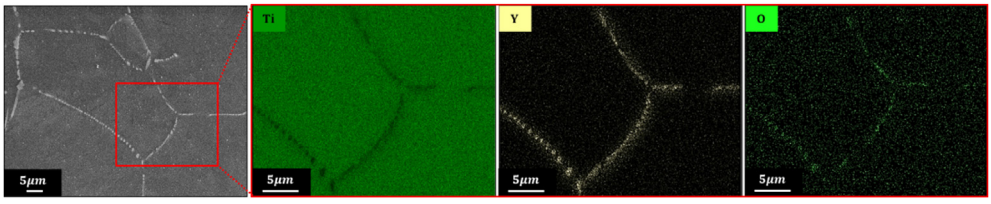

Fig. 4 – Microstructure of the Ti(0.1O)–1Y_2O_3 alloy rod ingot observed by FE-SEM. The leftmost figure is the BSE image, and the three figures on the right are the EDS mapping results of the red area in the BSE image.

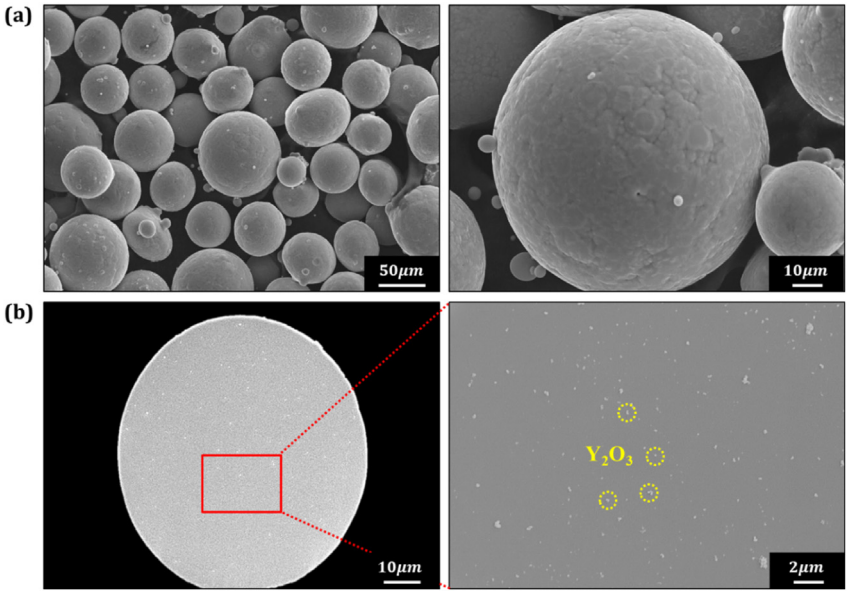

Fig. 5 – (a) The morphology and (b) cross-section microstructure of the Ti(0.1O)–1Y_2O_3 alloy powder observed by FE-SEM. In Fig. 5(b), the right figure is an enlarged microstructure of the red area in the cross-section microstructure of the powder on the left. The powder had a spherical shape, and fine Y_2O_3 particles were uniformly distributed inside the powder.

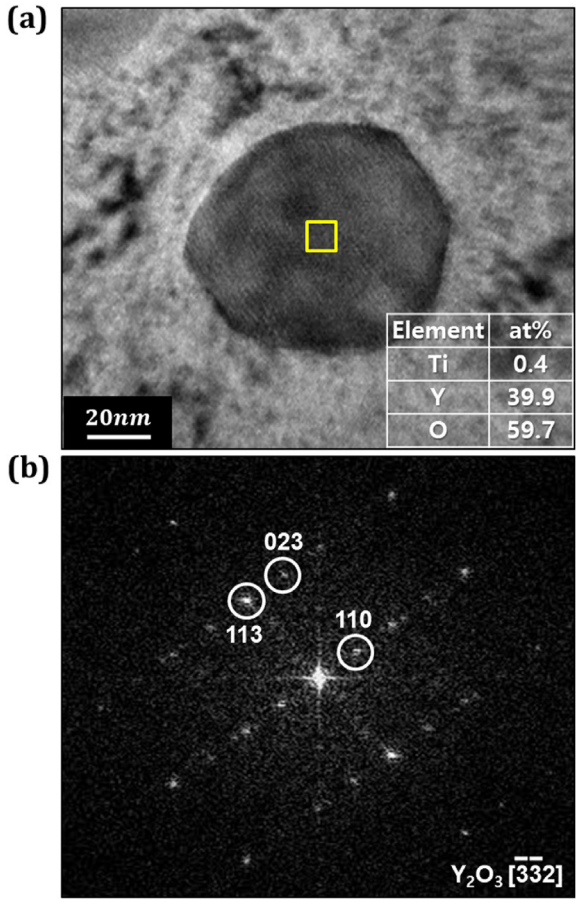

Fig. 6 – (a) High-resolution image and (b) diffraction pattern of the oxide particle insides the Ti(0.1O)–1Y_2O_3 alloy powder examined by FE-TEM. The table in Fig. 6(a) represents the chemical composition of oxide particle analyzed by EDS.

1Y_2O_3 alloy would be 0.79 and 0.31 wt%, respectively. Therefore, the equilibrium phase fraction was calculated according to the temperature in the Ti-0.79Y-0.31O (wt%) composition and the result is represented in Fig. 3. The red and black lines represent the α and β phases of Ti, respectively, and the blue and green lines represent the liquid and Y_2O_3 phase, respectively. The Y_2O_3 phase decomposed at 1730 K, which is lower than the solidus temperature (1930 K). In the alloy designed for this study, the Y_2O_3 will be decomposed and dissolved into molten Ti during melting and re-precipitated in the Ti matrix during cooling lower than 1730 K. Therefore, in order to confirm these thermodynamic approaches, experiments to fabricate the Ti(0.1O)–1Y_2O_3 alloy rod ingot and powder were performed.

Fig. 4 shows the microstructure of the Ti(0.1O)–1Y_2O_3 alloy rod ingot fabricated by VAR. The leftmost figure shows the microstructure observed by back-scattered electron (BSE) imaging mode, and the three figures on the right are the EDS mapping results of the red area in the BSE image. In the BSE image, a coarse white phase was precipitated along the grain boundaries of the Ti matrix, and it was confirmed as Y oxide from the EDS mapping results. Upon performing a point analysis of the white phase, its composition was 3.5Ti-38.6Y-57.9O (at%), closely identical to Y_2O_3. The melting temperature of Y_2O_3 is 2698 K, much higher compared to that of Ti (1941 K). However, based on the microstructure of the rod ingot, Y_2O_3 melted in molten Ti during melting in the VAR process and re-precipitated along the grain boundaries during cooling. This is because the Y_2O_3 is decomposed and dissolved into molten Ti at the melting of the Ti(0.1O)–1Y_2O_3 alloy rod ingot, according to the thermodynamic calculation results (Fig. 3).

Fig. 5 represents the morphology and microstructure of the Ti(0.1O)–1Y_2O_3 alloy powder fabricated through the EIGA process. In Fig. 5(a), the powder had a spherical shape applicable to the AM process. Looking at the morphology, no oxide particle was observed on the powder's surface. Fig. 5(b) shows the cross-section microstructures of the powder, where white-colored precipitates were present inside the powder. When the red area in the left figure is enlarged, fine precipitates are uniformly distributed inside the powder.

To analyze the phase of fine precipitates, the powder was examined using FE-TEM, and the results are shown in Fig. 6. Fig. 6(a) and (b) show the high-resolution image and diffraction pattern of the precipitate, respectively. From the TEM analysis, it was found that the precipitates with the size of 100 nm or less existed inside the powder. As the composition analysis result of the precipitate using EDS, its composition was 0.4Ti–39.9Y–59.7O (at%). From the diffraction pattern of the precipitate (Fig. 6(b)), the precipitate was also confirmed to be Y_2O_3. These microstructure analysis results prove that the powder with fine Y_2O_3 uniformly distributed inside can be fabricated in situ using the gas atomization method.

Fig. 7 shows a schematic of the in situ fabrication process of the ODS Ti powder. The Ti(0.1O)–1Y_2O_3 alloy rod ingot was prepared through the VAR. From the previous studies, the cooling rate in the gas atomization process is 10^4–10^5 K/s [29,30], and the cooling rate in the VAR process is 10–100 K/s [31]. The cooling rate in the gas atomization process is much faster than that in the VAR process. Based on the microstructure of the rod ingot (Fig. 4), Y_2O_3 was coarsely precipitated along the grain boundaries, and this microstructure was attributed to the relatively slow cooling rate in the VAR process. When the oxides are coarsely formed along the grain boundaries, it adversely affects the mechanical properties, and in particular, the toughness is rapidly deteriorated [32,33]. The Ti(0.1O)–1Y_2O_3 alloy powder was fabricated through the EIGA, and the coarse Y_2O_3 in the rod ingot was dissolved again into the molten Ti while melting. In the atomization process, high-pressure gas was sprayed on the molten Ti droplets to fabricate the powder, at this time, Y_2O_3 could be finely and uniformly precipitated inside the Ti powder by rapid cooling (Fig. 5).

By uniformly distributing oxides having a size of several tens of nm in the metal matrix, it is possible to secure excellent mechanical properties. To examine the hardness improvement by the dispersion of fine Y_2O_3 in the Ti matrix, the hardness of pure Ti and Ti(0.1O)–1Y_2O_3 powders was measured and the results are represented in Table 2. The hardness of the pure Ti powder was 187 HV, and the hardness of the Ti(0.1O)–1Y_2O_3 powder significantly increased to 311 HV. Through this, it was confirmed that the hardness improvement could be achieved by dispersing fine oxides in

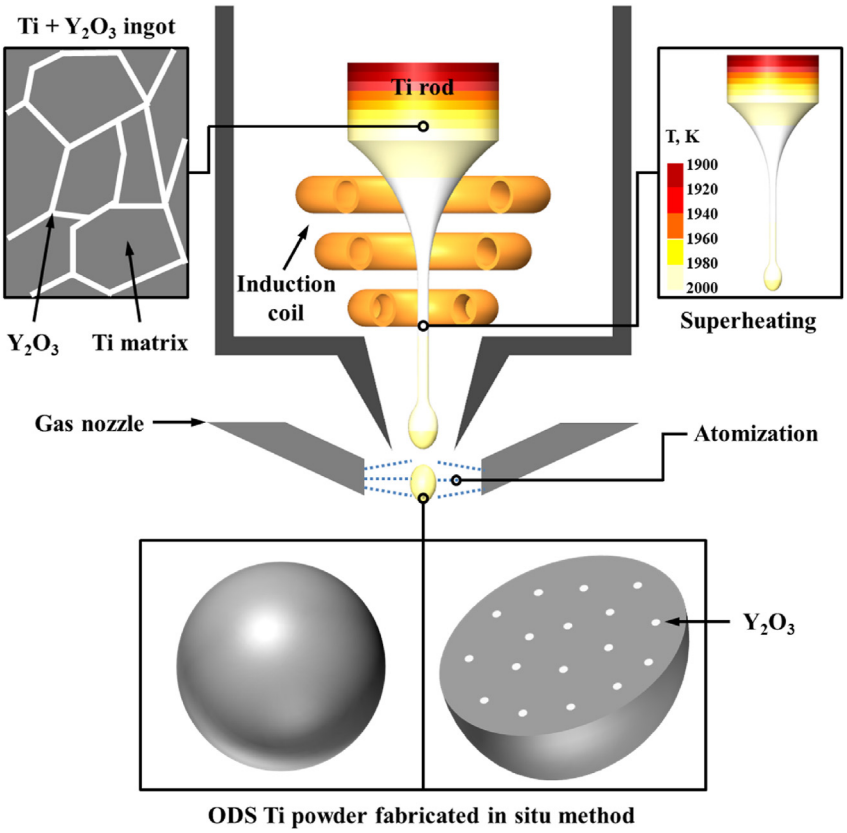

Fig. 7 – Schematic representing the in situ fabrication of the ODS Ti powder by the gas atomization method. The Y_2O_3 is coarsely precipitated along the grain boundary in the rod ingot, and it is finely and uniformly distributed inside powder by the difference of cooling rate in the VAR and EIGA processes.

Table 2 – Vickers hardness of the pure Ti and the Ti(0.1O)–1Y_2O_3 powders.

	Hardness [HV]
Pure Ti powder	187
Ti(0.1O)–1Y_2O_3 powder	311

the Ti matrix. If this ODS Ti powder applies to the AM process, although the powder is melt again by the laser, Y_2O_3 can be finely and uniformly distributed due to the rapid cooling rate in the AM process. Therefore, it is expected that the Ti components with high mechanical properties could be fabricated by adopting the ODS Ti powder developed in this study.

In general, the high temperature mechanical properties are improved by finely dispersing Y_2O_3 in the alloy matrix due to the high stability of the Y_2O_3 [34,35]. In the Ti–6Al–4V alloy, it has been reported that high temperature strength is significantly improved at 450 °C by the addition Y_2O_3 to the Ti–6Al–4V alloy [19]. Therefore, when fine Y_2O_3 oxides are dispersed in the Ti alloys, it is expected that high temperature properties are improved up to 400–500 °C. However, since the oxygen solubility of Ti is high, there is a possibility that Y_2O_3 oxides may be coarsened at a temperature higher than that. Therefore, further study is needed to precisely evaluate the mechanical properties at high temperatures of the ODS Ti alloys.

4. Conclusions

This study developed the technology for the in situ fabrication method of the spherical oxide dispersion strengthened (ODS) Ti powder. Through the thermodynamic analysis, it was derived that Y_2O_3 is dissolved in Ti melt during melting and precipitated upon cooling, and the ODS Ti alloy was designed in which 1 wt% Y_2O_3 was added to Ti with the O concentration of 0.1 wt%. Based on the thermodynamic calculation results, Y_2O_3 is completely decomposed and dissolved into molten Ti at the melting temperature of the Ti(0.1O)–1Y_2O_3 alloy. The Ti(0.1O)–1Y_2O_3 alloy rod ingot used for the electrode induction melting gas atomization (EIGA) process was fabricated through vacuum arc remelting (VAR), and Y_2O_3 was coarsely precipitated along the grain boundaries due to the slow cooling rate of VAR. The powder was prepared through EIGA, and the Y_2O_3 particles with a size of several tens of nm were uniformly distributed inside the powder due to the rapid cooling rate in the gas atomization process. Through this alloy design based on thermodynamics and experiments, it was confirmed that ODS Ti powder, where fine oxides are uniformly

distributed inside the Ti powder, can be fabricated by the in situ method.

Declaration of competing interest

The authors declare that they have no known competing financial interests or personal relationships that could have appeared to influence the work reported in this paper.

Acknowledgments

This research was supported by the Korea Institute of Industrial Technology (KITECH JA-23-0014) and the Creative Materials Discovery Program (No. NRF-2019M3D1A1079227) through the National Research Foundation of Korea (NRF) funded by Ministry of Science and ICT.

REFERENCES

[1] Jung JH, Choi Jh, Lee BS, Na TW, Kim HG, Park HK. Improvement of mechanical properties of cast pure titanium by repeated heat treatment. Mater Sci Technol 2019;35:248–52. https://doi.org/10.1080/02670836.2018.1495901.

[2] Park HK, Na TW, Park JM, H Kim Y, Kim GH, Lee BS, et al. Effect of cyclic heat treatment on commercially pure titanium part fabricated by electron beam additive manufacturing. J Alloys Compd 2019;796:300–6. https://doi.org/10.1016/j.jallcom.2019.04.335.

[3] Pan Y, Zhang J, Sun J, Liu Y, Zhang C, Li R, et al. Enhanced strength and ductility in a powder metallurgy Ti material by the oxygen scavenger of CaB_6. J Mater Sci Technol 2023;137:132–42. https://doi.org/10.1016/j.jmst.2022.07.042.

[4] Park HK, Ahn YK, Lee BS, Jung KH, Lee CW, Kim HG. Refining effect of electron beam melting on additive manufacturing of pure titanium products. Mater Lett 2017;187:98–100. https://doi.org/10.1016/j.matlet.2016.10.065.

[5] Na TW, Kim WR, Yang SM, Kwon Oh, Park JM, Kim GH, et al. Effect of laser power on oxygen and nitrogen concentration of commercially pure titanium manufactured by selective laser melting. Mater Char 2018;143:110–7. https://doi.org/10.1016/j.matchar.2018.03.003.

[6] Park HK, Na TW, Yang SM, Kim GH, Lee BS, Kim HG. Thermodynamic analysis of oxygen refining during electron-beam additive manufacturing of pure titanium products. Mater Lett 2019;236:106–8. https://doi.org/10.1016/j.matlet.2018.10.083.

[7] Revankar GD, Shetty R, Rao SS, Gaitonde VN. Wear resistance enhancement of titanium alloy (Ti–6Al–4V) by ball burnishing process. J Mater Res Technol 2017;6(1):13–32. https://doi.org/10.1016/j.jmrt.2016.03.007.

[8] Niinomi M. Mechanical biocompatibilities of titanium alloys for biomedical applications. J Mech Behav Biomed Mater 2008:30–42. https://doi.org/10.1016/j.jmbbm.2007.07.001.

[9] Narayana PL, Kim SW, Hong JK, Reddy NS, Yeom JT. Tensile properties of a newly developed high-temperature titanium alloy at room temperature and 650 °C. Mater Sci Eng, A 2018;718:287–91. https://doi.org/10.1016/j.msea.2018.01.113.

[10] Singh R, Prakash U, Kumar D, Laha K. Nano oxide particles in 18Cr oxide dispersion strengthened (ODS) steels with high yttria contents. Mater Char 2022;189:111936. https://doi.org/10.1016/j.matchar.2022.111936.

[11] Klueh RL, Shingledecker JP, Swindeman RW, Hoelzer DT. Oxide dispersion-strengthened steels: a comparison of some commercial and experimental alloys. J Nucl Mater 2005;341:103–14. https://doi.org/10.1016/j.jnucmat.2005.01.017.

[12] Park CW, Byun JM, Choi WJ, Lee SY, Kim YD. Improvement of high temperature mechanical properties of Ni-based oxide dispersion strengthened alloys by preferential formation of Y-Ti-O complex oxide. Mater Sci Eng, A 2019;740–741:363–7. https://doi.org/10.1016/j.jnucmat.2005.01.017.

[13] Xu R, Geng Z, Wu Y, Chen C, Ni M, Li D, et al. Microstructure and mechanical properties of in-situ oxide-dispersion-strengthened NiCrFeY alloy produced by laser powder bed fusion. Adv Powder Mater 2022;1:100056. https://doi.org/10.1016/j.apmate.2022.100056.

[14] Qiu C. A new approach to synthesise high strength nano-oxide dispersion strengthened alloys. J Alloys Compd 2019;790:1023–33. https://doi.org/10.1016/j.jallcom.2019.03.221.

[15] Liu X, Yin H, Xu Y. Microstructure, mechanical and tribological properties of oxide dispersion strengthened high-entropy alloys. Materials 2017;10(11):1312. https://doi.org/10.3390/ma10111312.

[16] Wang J, Yuan W, Mishra RS, Charit I. Microstructure and mechanical properties of friction stir welded oxide dispersion strengthened alloy. J Nucl Mater 2013;432:274–80. https://doi.org/10.1016/j.jnucmat.2012.08.001.

[17] Zhong SY, Ribis J, Klosek V, Carlan Yd, Lochet N, Ji V, et al. Study of the thermal stability of nanoparticle distributions in an oxide dispersion strengthened (ODS) ferritic alloys. J Nucl Mater 2012;428:154–9. https://doi.org/10.1016/j.jnucmat.2011.12.028.

[18] Krautwasser P, Filemonowicz AC, Widera M, Carsughi F. Thermal stability of dispersoids in ferritic oxide-dispersion-strengthened alloys. Mater Sci Eng, A 1994;177:199–208. https://doi.org/10.1016/0921-5093(94)90491-X.

[19] Li A, Ma S, Yang Y, Zhou S, Shi L, Liu M. Microstructure and mechanical properties of Y_2O_3 reinforced Ti6Al4V composites fabricated by spark plasma sintering. J Alloys Compd 2018;768:49–56. https://doi.org/10.1016/j.jallcom.2018.07.229.

[20] Li Y, Han C, Zhu X, Wen C, Hodgson P. Osteoblast cell response to nanoscale SiO2/ZrO2 particulate-reinforced titanium composites and scaffolds by powder metallurgy. J Mater Sci 2012;47:4410–4. https://doi.org/10.1007/s10853-012-6295-4.

[21] Aghamiri SMS, Oono N, Ukai S, Kasada R, Noto H, Hishinuma Y, et al. Microstructure and mechanical properties of mechanically alloyed ODS copper alloy for fusion material application. Nucl Mater Energy 2018;15:17–22. https://doi.org/10.1016/j.nme.2018.05.019.

[22] Macía E, Junceda AG, Serrano M, Hong SJ, Campos M. Effect of mechanical alloying on the microstructural evolution of a ferritic ODS steel with (Y–Ti–Al–Zr) addition processed by Spark Plasma Sintering (SPS). Nucl Eng Technol 2021;53:2582–90. https://doi.org/10.1016/j.net.2021.02.002.

[23] Park KB, Park JY, Kim YD, Choi JI, Im HT, Kang JW, et al. Study on hydrogen absorption and surface properties of TiZrVNbCr high entropy alloy. Intermetallics 2021;130:107074. https://doi.org/10.1016/j.intermet.2020.107074.

[24] Lee WH, Na TW, Yi KW, Yang SM, Kang JW, Kim HG, et al. Thermodynamic analysis of oxidation during selective laser melting of pure titanium. Rapid Prototyp J 2020;26(8):1401.

[25] Cai C, Radoslaw C, Zhang J, Yan Q, Wen S, Song B, Shi Y. In-situ preparation and formation of TiB/Ti-6Al-4V

nanocomposite via laser additive manufacturing: microstructure evolution and tribological behavior. Powder Technol 2019;342:73–84. https://doi.org/10.1016/j.powtec.2018.09.088.

[26] Holland TJB. Dependence of entropy on volume for silicate and oxide minerals: a review and a predictive model. Am Mineral 1989;74:5–13.

[27] Kojima Y, Yamaguchi M. Thermodynamic analysis of metal oxides, metal peroxides and metal hydrides. Mater Today Commun 2022;33:104691. https://doi.org/10.1016/j.mtcomm.2022.104691.

[28] Hautaniemi JA, Herø H, Juhanoja JT. On the bonding of porcelain on titanium. J Mater Sci Mater Med 1992;3:186–91. https://doi.org/10.1016/j.mtcomm.2022.104691.

[29] Martín A, Jiménez CMC, Prado MTP. Gas atomization of γ-TiAl alloy powder for additive manufacturing. Adv Eng Mater 2020:1900594. https://doi.org/10.1002/adem.201900594.

[30] Wu J, Xia M, Wang J, Zhao B, Ge C. Effect of electrode induction melting gas atomization on powder quality: satellite formation mechanism and pressure. Mater 2023;16:2499. https://doi.org/10.3390/ma16062499.

[31] Wang F, Yuan T, Li R, Lin S, Xie Z, Li L, et al. Comparative study on microstructures and mechanical properties of ultra ductility single-phase Nb40Ti40Ta20 refractory medium entropy alloy by selective laser melting and vacuum arc melting. J Alloys Compd 2023;942:169065. https://doi.org/10.1016/j.ijpvp.2018.04.004.

[32] Arora KS, Pandu SR, Shajan N, Pathak P, Shome M. Microstructure and impact toughness of reheated coarse grain heat affected zones of API X65 and API X80 linepipe steels. Int J Pres Ves Pip 2018;163:36–44. https://doi.org/10.1016/j.ijpvp.2018.04.004.

[33] Fang CZ, Basoalto HC, Anderson MJ, Li HY, Williams SJ, Bowen P. A numerical study on the influence of grain boundary oxides on dwell fatigue crack growth of a nickel-based superalloy. Mater Sci Technol 2022;104:224–35. https://doi.org/10.1016/j.jmst.2021.06.045.

[34] Wang M, Han HN, Han CH, Kim WG, Jang JS. Microstructural investigation of oxide dispersion strengthened alloy 617 after creep rupture at high temperature. Mater Char 2018;139:11–8. https://doi.org/10.1016/j.matchar.2018.02.031.

[35] Miller MK, Russell KF, Hoelzer DT. Characterization of precipitates in MA/ODS ferritic alloys. J Nucl Mater 2006;351:261–8. https://doi.org/10.1016/j.jnucmat.2006.02.004.